HARD X-RAY IMAGING OF SOLAR FLARES USING INTERPOLATED VISIBILITIES

Anna Maria Massone[1], A. Gordon Emslie[2], G. J. Hurford[3], Marco Prato[1,4], Eduard P. Kontar[5], and Michele Piana[1,6]
[1] CNR-INFM LAMIA, via Dodecaneso 33, I-16146 Genova, Italy; massone@ge.infm.it
[2] Department of Physics, Oklahoma State University, Stillwater, OK 74078, USA; gordon.emslie@okstate.edu
[3] Space Sciences Laboratory, University of California at Berkeley, 7 Gauss Way, Berkeley, CA 94710, USA; ghurford@ssl.berkeley.edu
[4] Dipartimento di Matematica, Università di Modena e Reggio Emilia, via Campi 213/b, I-41100 Modena, Italy; marco.prato@unimore.it
[5] Department of Physics & Astronomy, The University, Glasgow G12 8QQ, UK; eduard@astro.gla.ac.uk
[6] Dipartimento di Informatica, Università di Verona, Cà Vignal 2, Strada le Grazie 15, I-37134 Verona, Italy; michele.piana@univr.it
Received 2009 April 29; accepted 2009 August 20; published 2009 September 15

ABSTRACT

RHESSI produces solar flare images with the finest angular and spectral resolutions ever achieved at hard X-ray energies. Because this instrument uses indirect, collimator-based imaging techniques, the "native" output of which is in the form of "visibilities" (two-dimensional spatial Fourier components of the image), the development and application of robust, accurate, visibility-based image reconstruction techniques is required. Recognizing that the density of spatial-frequency (u, v) coverage by *RHESSI* is much sparser than that normally encountered in radio astronomy, we therefore introduce a method for image reconstruction from a relatively sparse distribution of sampled visibilities. The method involves spline interpolation at spatial frequencies less than the largest sampled frequency and the imposition of a positivity constraint on the image to reduce the ringing effects resulting from an unconstrained Fourier transform inversion procedure. Using simulated images consisting both of assumed mathematical forms and of the type of structure typically associated with solar flares, we validate the fidelity, accuracy, and robustness with which the new procedure recovers input images. The method faithfully recovers both single and multiple sources, both compact and extended, over a dynamic range of $\sim 10 : 1$. The performance of the method, which we term as `uv_smooth`, is compared with other *RHESSI* image reconstruction algorithms currently in use and its advantages summarized. We also illustrate the application of the method using *RHESSI* observations of four solar flares.

Key words: methods: data analysis – Sun: flares – Sun: X-rays, gamma rays – techniques: image processing

Online-only material: color figures

1. INTRODUCTION

Data from *RHESSI* (Lin et al. 2002) have resulted in hard X-ray (and even some gamma-ray) images that combine the finest angular and spectral resolutions ever achieved at these energies. The resulting *imaging spectroscopy* capability provides a powerful tool with which to explore the underlying physics of particle acceleration and transport in solar flares.

RHESSI imaging is accomplished through the use of a set of nine rotating modulation collimators (RMCs) whose FWHM resolution is logarithmically spaced between 2.3 and 183 arcsec. Each RMC rapidly time modulates the detected photon flux, thereby encoding imaging information in the pattern of these time variations. Image reconstruction algorithms are then used to convert the resulting light curves into X-ray maps in the energy range of interest. Most image reconstruction algorithms begin with count rates accumulated into a large number ($\sim 10^3$–10^6) of short time bins of ~ 10–100 milliseconds each. Various strategies, described by Hurford et al. (2002), are then used to determine the image corresponding to these time-binned data. These include the following.

1. Clean (Hogbom 1974), which starts from a back-projected map and reduces sidelobes by successively subtracting the point response function of the brightest points in the field of view.
2. Forward-fit (Aschwanden 2002), which assumes a parametric functional form (e.g., a two-dimensional Gaussian) for the source, and determines the best-fit parameters through comparison of the predicted modulation light curves with those observed.

3. Pixon (Piña & Puetter 1993), which minimizes image complexity by smoothing the image model locally as much as the data allow, thus reducing the number of independent elements in the image.

Since *RHESSI* images are typically based on $\sim 10^3$–10^5 counts, these image reconstruction algorithms typically deal with a relatively large number of time series, each element of which has limited statistical significance. An alternative approach, described by G. J. Hurford et al. (2009, in preparation) exploits the fact that the instantaneous amplitude and phase of each time-modulated light curve directly measure a specific spatial Fourier component, or *visibility*, of the source. Specifically, each RMC measures visibilities with a spatial frequency corresponding to its angular resolution and with a position angle that varies continuously as the spacecraft rotates. In the spatial frequency (u, v) plane, the measurements thus correspond to a set of circles, with logarithmically spaced radii corresponding to the (inverse) spatial resolution of the RMCs (see Figure 1). In principle, all the imaging information in the modulated light curves is encoded in these visibilities.

Representing the input data in terms of a limited number ($\sim 10^2$) of statistically independent visibilities, rather than as a series of sparsely populated light curves, has several advantages. First, statistical uncertainties in the visibilities can be readily calculated and, for simple sources, propagated into statistical uncertainties in the source parameters. Second, since the visibilities are linearly related to the observed count rate data, they can be linearly combined and/or weighted (as a function of time or energy, for example) to suit the user's purposes.
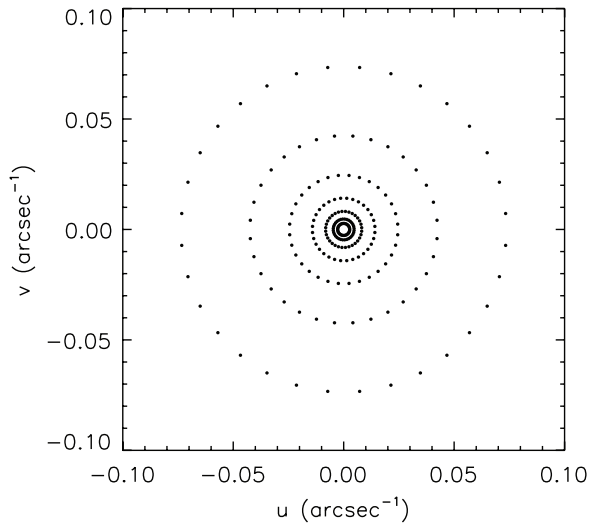
Figure 1. Sampled spatial frequency points. Visibilities from each collimator (three through nine) are sampled at 32 spatial frequency points, each lying on a circle in the spatial frequency—(u, v) plane.

Image reconstruction from measured visibilities has a long and successful history in radio astronomy, where the visibilities are determined through interferometry. However, modern radio interferometers usually provide much denser coverage in the (u, v) plane than provided by *RHESSI*'s nine RMCs. As a result, the highly developed algorithms in this field (e.g., Thomson et al. 2001) are not necessarily well suited to image reconstruction from *RHESSI* visibilities.

To date, three algorithms have been adapted to convert *RHESSI* visibilities into maps. The most basic of these is a "back-projection" algorithm that corresponds to a direct Fourier inversion of the measured visibilities, yielding a convolution of the actual source and the instrumental point-response function. Such a "dirty map" has significant sidelobes and is therefore of limited usefulness. The second method is the "MEM–NJIT" maximum entropy routine (Bong et al. 2006), the application of which is not always successful (Dennis & Pernak 2009). The third method is a visibility based forward fitting routine that determines the best-fit values of the parameters corresponding to assumed simple functional forms for the source. While this algorithm does yield well-determined statistical errors, its applicability is limited to sources whose morphology is well matched to the prescribed functional form.

This paper fills a need by introducing a robust, widely applicable algorithm for reconstructing images from *RHESSI* visibilities. It proceeds by smoothing the observed visibilities in the spatial frequency plane, thereby providing a much larger set of Fourier components to be used in performing the Fourier inversion that leads to the final image. The method consists of a two-step process (Section 2) consisting of

1. interpolation to generate a smooth continuum of visibilities within the disk in the (u, v) plane spanned by the available data; and
2. the imposition of image positivity through a Fast Fourier Transform (FFT)-based iterative method.

As we show in Section 3, using synthetic images of a series of physically plausible source maps, the method typically reproduces the true form of the source with a high degree of accuracy, fidelity, and robustness, and in a very computationally efficient manner. In Section 4, we apply the technique to four

flares on 2002 February 20, 2002 April 15, 2004 August 31, and 2002 July 23, and we critically compare the results of our method with those from the MEM–NJIT (Bong et al. 2006) algorithm in the key areas of *location, photometry, size, shape*, and *dynamic range*.

2. THE UV_SMOOTH IMAGE RECONSTRUCTION METHOD

In this section, we discuss the essential steps of the method. More details may be found in the source IDL code `uv_smooth` that has been incorporated in the SolarSoftWare (SSW) tree (Schwartz et al. 2002).

2.1. The Sparseness of the RHESSI Visibility Data

RHESSI's nine RMCs have angular FWHMs starting at $\alpha_1 \simeq 2.26$ arcsec and increasing in geometric steps of $\sqrt{3}$ to $\alpha_9 \simeq 183$ arcsec. As the spacecraft rotates, these RMCs sample the spatial frequency (u, v) domain along nine circles with radii from $R_9 (= 1/2\alpha_9 \simeq 0.0027$ arcsec^{-1}) to $R_1 (= 1/2\alpha_1 \simeq 0.221$ arcsec^{-1}); the radii of nearest-neighbor circles are related through $R_i = \sqrt{3} \, R_{i+1}$.

For the tests reported herein, we have chosen not to use the (u, v) points sampled by collimators 1 and 2, restricting attention instead only to collimators 3 through 9. This is because the detector associated with collimator 2 has had intermittent technical problems, requiring a large (factor of 3) interpolation across the spatial frequency gap between collimators 1 and 3, $\sqrt{3}$ times larger than the intervals over which the other interpolations are performed. (There is, however, nothing in the algorithm that would preclude the application of the method to data from collimators 1 and 2 when warranted by the high-quality detector 2 data obtained later in the mission.)

Although the modulation profile for each collimator reflects the visibilities measured over a continuum of orientations, it is convenient to make measurements at a discrete set of azimuthal angles. The choice of azimuthal spacing of such measurements is influenced by two conflicting requirements. On one hand, the ratio of the imaging field of view to the spatial period of a given collimator defines a maximum azimuthal spacing that satisfies the Nyquist–Shannon theorem (expressed in polar coordinates) for adequate sampling in the (u, v) plane. On the other hand, a minimum spacing in azimuth is imposed by the requirement that there be adequate sampling of a modulation cycle. For some methods (e.g., forward fit, maximum entropy), it is further required that each measured visibility be statistically independent; however, this is *not* required for the algorithm to be developed here. In the simulations of the next two sections, we will assume the availability of 32 visibilities for each detector.

2.2. Visibility Interpolation within the Sampling Domain

The visibilities measured by *RHESSI* are discretely arranged around concentric circles in the (u, v) plane—see Figure 1; this results in images that contain substantial sidelobe artifacts, typically in the form of concentric rings. Our new approach begins by estimating the visibility function $V(u, v)$ across the whole disk $\rho \leqslant R_3$ spanned by the sampled data points, including not only (u, v) points satisfying $R_9 \leqslant \rho \leqslant R_3$, but also those with $\rho < R_9$. (The extension to this central region in the (u, v) plane is plausible since the associated spatial frequencies correspond to very large spatial scales $\gtrsim 180''$, beyond which little emission and/or structure is expected.) From this we construct visibility values on an equally spaced Cartesian

grid of points[7]. Using these uniformly spaced visibility values in an FFT image reconstruction algorithm produces images in which many of the undesirable sidelobes associated with sparse (u, v) sampling are suppressed.

Three different two-dimensional interpolation techniques were studied, namely:

1. a linear polynomial interpolation method, involving a simple linear triangulation of the sampled visibility data points;
2. a quintic polynomial interpolation method, using linear combinations of all functions of the form $u^\alpha v^\beta$, where α and β are whole numbers satisfying $\alpha + \beta \leqslant 5$; and
3. the IDL-based thin-plate spline interpolation algorithm `grid_tps` (Wahba 1990), a generalization of the standard linear cubic spline procedure which finds the "locally minimally bent" smooth surface passing through all sampled points.

2.3. Application to Simple Sources

It is instructive to consider the fidelity and accuracy of the images generated using various interpolation schemes for a rather simple simulated source, corresponding to the circular two-dimensional Gaussian

$$I(x, y) \sim \frac{A}{2\pi\,\sigma^2} \exp\left[-\frac{(x-x_1)^2 + (y-y_1)^2}{2\,\sigma^2}\right], \quad (1)$$

where A (an arbitrary value) is the total flux emitted by the source, and we have set the width of the source $\sigma = 4''$, somewhat greater than the angular resolution of the finest collimator. The corresponding visibilities $V(u,v)$ are given by

$$\begin{aligned} V(u, v) &= \int_{x=-\infty}^{\infty} \int_{y=-\infty}^{\infty} I(x, y)\, e^{2\pi i(u[x-x_0]+v[y-y_0])}\, dx\, dy \\ &= A\, e^{-2\pi^2\sigma^2\,(u^2+v^2)}\, e^{2\pi i[u(x_1-x_0)+v(y_1-y_0)]}, \quad (2) \end{aligned}$$

where the phase center (x_0, y_0) is displaced by an arbitrary non-zero distance from the center (x_1, y_1) of the Gaussian. We evaluated $V(u, v)$ at only the sampled (u, v) points shown in Figure 1; these "raw" visibilities were then used as input to the various interpolation methods[8].

Figure 2 shows a comparison of the results obtained using these various interpolation methods. Rows (a) and (b) both use a back-projection algorithm (with natural and uniform weighting, respectively); this method employs only the directly measured visibilities, with the resulting map normalized to the peak of the intensity profile. Row (c) corresponds to the linear interpolation method, row (d) to the quintic polynomial interpolation method, and row (e) to the thin-plate spline algorithm.

Radial cuts across the source structure (the right column of Figure 2) show that a very significant improvement in image quality is obtained when interpolated, rather than raw, visibilities are used. Further, because of the added feature of overall smoothness in the *visibility* surface (the left column of Figure 2) when using the plate-spline interpolation method, we

hereafter employ this method as our interpolation algorithm. We point out that this algorithm (as for any interpolation approach) has the added advantage that the smoothed visibility surface representing the input data to the FFT algorithm *passes through the measured visibility points exactly*; hence, the measured visibilities corresponding to the recovered source in row (e) of Figure 2 are *identical* to those for the original source. Thus, while the method provides smoothly interpolated *estimates* of visibilities for (u, v) points that are *not* sampled by the instrument, it does so by maintaining the *exact* values of the visibilities for the (u, v) points that *are* sampled.

2.4. Implementation of Positivity Constraint

Even after interpolation, the visibility information still covers only a limited portion of the (u, v) plane; there is no (high-frequency) visibility information outside the disk of radius $\rho = R_3$. Without this high-frequency information, it is impossible to faithfully realize the true (Gaussian) Fourier transform, which contains *all* spatial frequencies. The high-frequency cutoff at $\rho = R_3$ is manifested both as an overestimation of the size of the reconstructed image (due to convolution of the true source size with the finite width of the instrumental point-spread function (PSF)) and in the appearance of residual "ringing" oscillations (due to truncation of Fourier-space information). Both these features are evident throughout all the image reconstructions in Figure 2. To reduce the "ringing" oscillations (with their associated unphysical negative values for the source intensity), we extend the method by including a constraint which acts to force positivity throughout the source image. It has been noted (Youla 1987) that the imposition of such a constraint does indeed act to produce the desired extrapolation of the visibility surface beyond the upper frequency cutoff.

The method used (Piana & Bertero 1997) is a successive-approximation iterative scheme, driven by the competing factors of image positivity and compatibility of the corresponding visibilities with the smooth visibility surface derived in the previous subsection. Enforcing positivity at each point in the image acts not only to alter the visibility surface within $\rho \leqslant R_3$ but also has the effect of slightly increasing the total flux in the image, i.e., the visibility $V(0, 0) = A$ (Equation (2)). To counter the latter effect, at each step the total flux in the image is renormalized to its actual value by setting all visibility components $V(u, v)$ to $\min[V(u, v), A]$. The iteration scheme typically converges after about a dozen iterations; it is terminated at an acceptable level of the χ^2 measuring the difference between the measured visibility values and their calculated counterparts. The implementation of the iterative scheme is made computationally effective by the use of an FFT routine to perform the required forward and backward Fourier transforms.

The results of this scheme are illustrated in Figure 3. Compared to the interpolation-only results (the center column of Figure 2), we see a noticeable reduction of the ringing effects outside the true source. As can be seen in the top panel of column (b) of Figure 3, the method produces a visibility surface that gradually tapers to zero outside $\rho = R_3$, rather than the abrupt falloff evidenced in the visibility surface of the left column of Figure 2.

The top panel of column (c) of Figure 3 shows a radial cut through the *visibility surface*. The originally sampled (measured) visibilities are shown as open squares, while the interpolated visibilities are shown as points (with 1σ error bars). Despite the fact that the iteration-incorporating-positivity

---

[7] This is similar to the gridding process in radio interferometry (Thomson et al. 2001). However, in that case, gridding often involves averaging densely sampled (u, v) points rather than interpolation.

[8] To conform with the requirements of the MEM–NJIT algorithm, the magnitude of the associated uncertainties was also provided, however, artificial data noise was *not* added in these simulations.
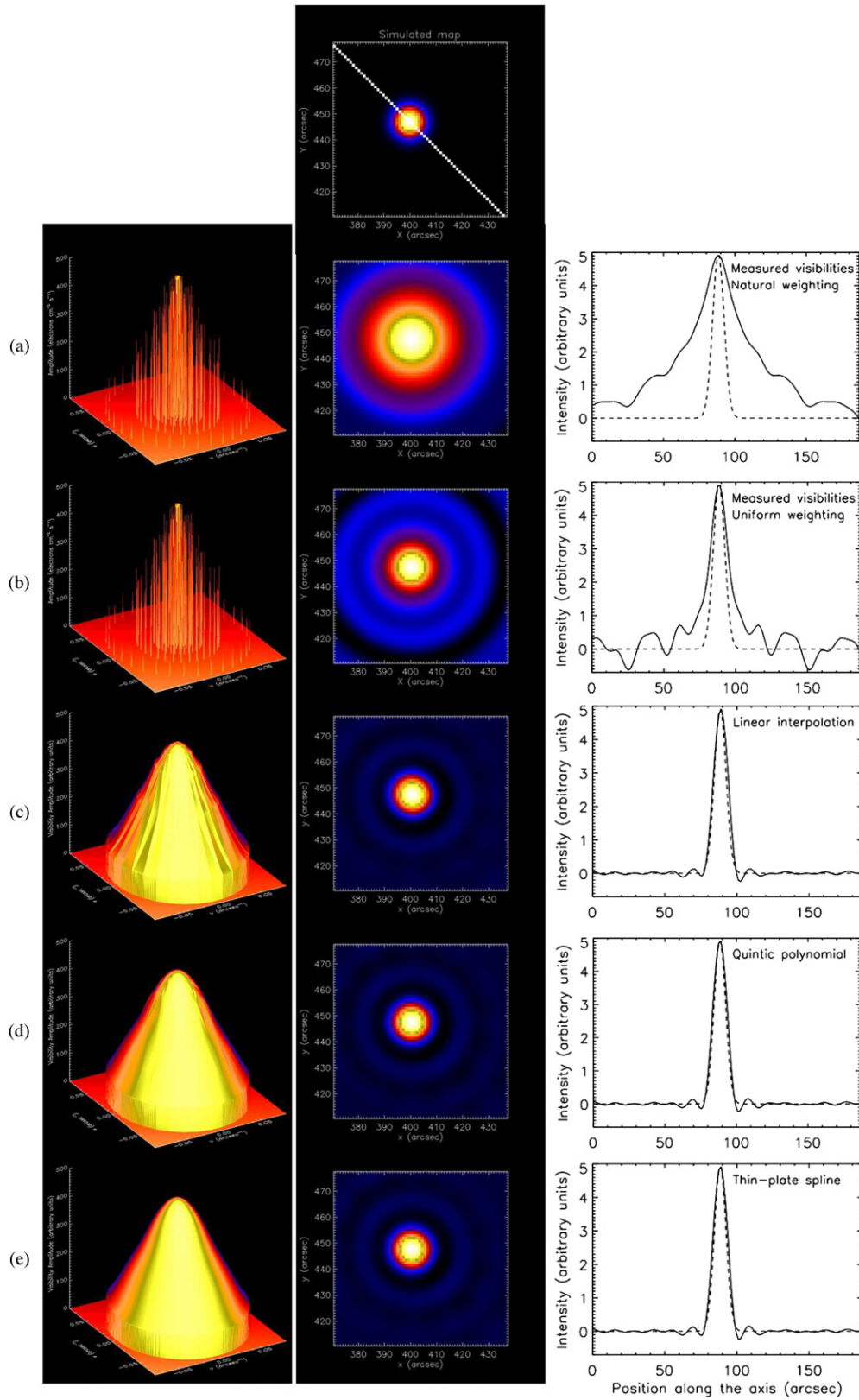
Figure 2. Comparison of interpolation methods for a circular Gaussian source. Topmost panel: an image of the original source. The next five rows show (left panels) the amplitudes of the visibilities used, (middle panels) the corresponding images, and (right panels) radial intensity profiles (solid line) along the line from source center to the bottom right corner of the frame, compared with that corresponding to the original source (dashed line). Rows (a) and (b): back-projection algorithm (with natural and uniform weighting, respectively); Row (c): linear interpolation method; Row (d): quintic polynomial interpolation method; Row (e): thin-plate spline algorithm.

(A color version of this figure is available in the online journal.)

Figure 3. Results from iterative method with positivity constraint. Column (a): the original synthetic image. Column (b): the visibility surface (upper panel) and image (lower panel) corresponding to the final step of the iterative method. Column (c), upper panel: the solid line shows a cut through the origin of the visibility surface. The originally sampled (measured) visibilities are shown as open squares, while the interpolated visibilities are shown as points (with 1σ error bars). The solid dots represent a zero-padding outside the range of the sampled data. Column (c), lower panel: the solid line shows the same radial cut through the image as in Figure 2, compared to the same cut (dashed line) through the original source.

(A color version of this figure is available in the online journal.)

method results in values of the visibilities at the sampled (u, v) points that are no longer *exactly* equal to the measured values, the visibility surface is still an acceptable fit to the data, given the observational uncertainties.

The lower panel of column (c) of Figure 3 is a radial cut across the corresponding *image*; compared to the cuts shown in Figure 2, we see that the ringing is strongly suppressed. The method reproduces the location of the peak intensity exactly and determines the peak source intensity to within 0.2%. Although the method overestimates the source size (FWHM) by some 15%, this is an inescapable manifestation of the instrument PSF, common to all image reconstruction techniques. As discussed by Dennis & Pernak (2009), it is readily compensated for by subtracting the PSF in quadrature.

3. VALIDATION OF THE ALGORITHM USING SIMULATED DATA

We hereafter term the visibility-based interpolation/ extrapolation algorithm described in the previous section as `uv_smooth`. Before applying it to actual data, it is important to assess its ability to reproduce plausible source forms, especially compared to other visibility-based image reconstruction methods such as MEM–NJIT (Bong et al. 2006) and `hsi_vis_fwdfit`. To do this, we use a variety of simulated data sets. For the first set of tests, we used sources described by mathematical forms. However, recognizing that actual solar flare images have a less-idealized amorphous structure, we also tested the algorithm using simulated data derived from hard X-ray images of actual solar flare events, prior to application of the method to actual data in Section 4.

3.1. Tests Using Functional Forms

The first two tests are aimed at a quantitative evaluation of the ability to reconstruct the locations, intensities, and sizes of multiple compact sources, and in particular to compare the results with those obtained with the MEM–NJIT algorithm. In subsequent tests (Section 4), we will compare the results from `uv_smooth` with the results using `hsi_vis_fwdfit` for somewhat different source geometries.

The first test extends the results of Figure 2 to the full `uv_smooth` method (results reproduced in the top row of Figure 4). The spatial frequency corresponding to the footpoint size is comparable to the highest spatial frequency sampled. MEM–NJIT underestimates the peak intensity by 8% and overestimates the width (FWHM) by 3% (compared to a 0.2% underestimate and 15% overestimate, respectively, for `uv_smooth`).

The second test, shown in the bottom row of Figure 4, involves *two* circular Gaussian sources, each with the same size and brightness, and separated by a few source widths σ; the results are shown in the bottom row of Figure 4. Both MEM–NJIT and `uv_smooth` reproduce well the *locations* (both absolute and relative) of the two Gaussian sources. Both methods also reproduce the *relative* intensities of the two sources; however, they underestimate the peak intensity of each, by some 5% and 7%, respectively. MEM–NJIT underestimates the source *widths* (FWHM) by some (3–6)%. It is apparent from Figure 4 that `uv_smooth` somewhat overestimates the width of the two sources by ~10%; however, use of FWHM is not appropriate since the sources are not resolved separately at the half-maximum level.
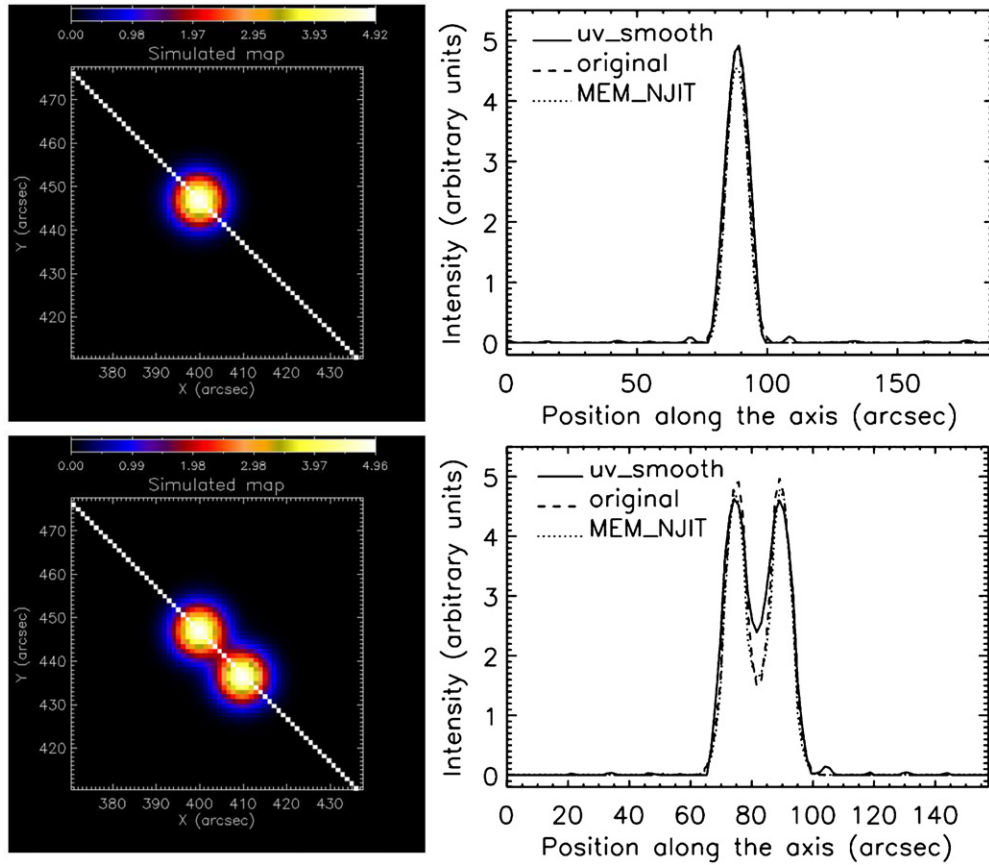
Figure 4. Comparison of image reconstruction methods for two simulated source maps. Top row: single circular Gaussian functional form (cf. Figure 2); Bottom row: double circular Gaussian functional form. The left column shows images of the simulated source maps. The right column shows the intensity profiles along the lines shown in the respective image panel, constructed using both MEM–NJIT (dotted) and the `uv_smooth` method (solid); the intensity profile from the original source is also shown (dashed). The field of view is (64 arcsec × 64 arcsec).

(A color version of this figure is available in the online journal.)

Motivated by this last result, the third test addresses the ability of `uv_smooth` to image multiple sources with *varying* brightness ratios; it tests the ability of the method to deal with a significant dynamic range of sources in the observed image plane. To this end, we extended the double-circular-Gaussian test to include sources with the same size σ (= 4 arcsec), but with brightness ratios b varying from 1 to 0.02. Figure 5 demonstrates the effectiveness of MEM–NJIT and `uv_smooth` in the reconstruction of such images. The left column of the figure shows the images reconstructed by `uv_smooth`, while the right column shows one-dimensional plots of the intensity along the line between the peaks of the two sources, using both MEM–NJIT and `uv_smooth` methods.

Again, both MEM–NJIT and `uv_smooth` faithfully recover the positions of both sources in all cases. For sources with actual brightness ratios ($b = 1, 0.2, 0.1, 0.02$), the MEM–NJIT method recovers values $b_{MEM} = (0.97, 0.24, 0.13, 0.006)$, while `uv_smooth` produces $b_{uvsmooth} = (0.99, 0.24, 0.15, 0.07)$. Thus, for moderate values of $b \gtrsim 0.1$, both methods overestimate the brightness of the weaker source, by ~20% ($b = 0.2$) and ~(30–50)% ($b = 0.1$). For $b = 0.02$, `uv_smooth` overestimates the brightness of the weaker source by a factor of ~3.5, while MEM–NJIT *under*estimates it by a factor of ~3, to the point where the weaker source is not discernable above the noise level. The dynamic range over which the fainter source can be determined using `uv_smooth` with reasonable certainty and accuracy is therefore ~10:1.

It must be emphasized that the results above represent the *best* results obtained from our MEM–NJIT simulations; for example, at low total count values the results are significantly degraded and may not even converge at all. Thus, although the MEM–NJIT method *can* produce a somewhat more faithful (compared to `uv_smooth`) reproduction of an image containing multiple compact sources, it may also perform more poorly (or even not at all). By contrast, the `uv_smooth` method produces reliable images at all values of the total count.

3.2. Tests based on Solar Flare Maps

Of course, actual solar flare images are in general only approximately represented by exact mathematical forms such as Equation (1). The next series of tests are aimed at assessing the ability of different methods to recover the morphology of features likely to be associated with actual flare events, and hence the ability of the method to image extended sources. We constructed images of two solar flares, one (2002 February 20, 11:06:02–11:06:34 UT, GOES C9.6) exhibiting a "double footpoint" structure very similar to the double-circular-Gaussian example of the previous subsection, and one (2004 August 31, 05:33:00–05:38:00 UT, GOES M1.4) exhibiting a more extended source, in all likelihood an extended coronal source (Xu et al. 2008). To provide a testing environment that is not biased toward any particular algorithm, the images used as "actual" sources were constructed using both "traditional" (e.g., MEM–NJIT) methods and `uv_smooth` itself. In each case,
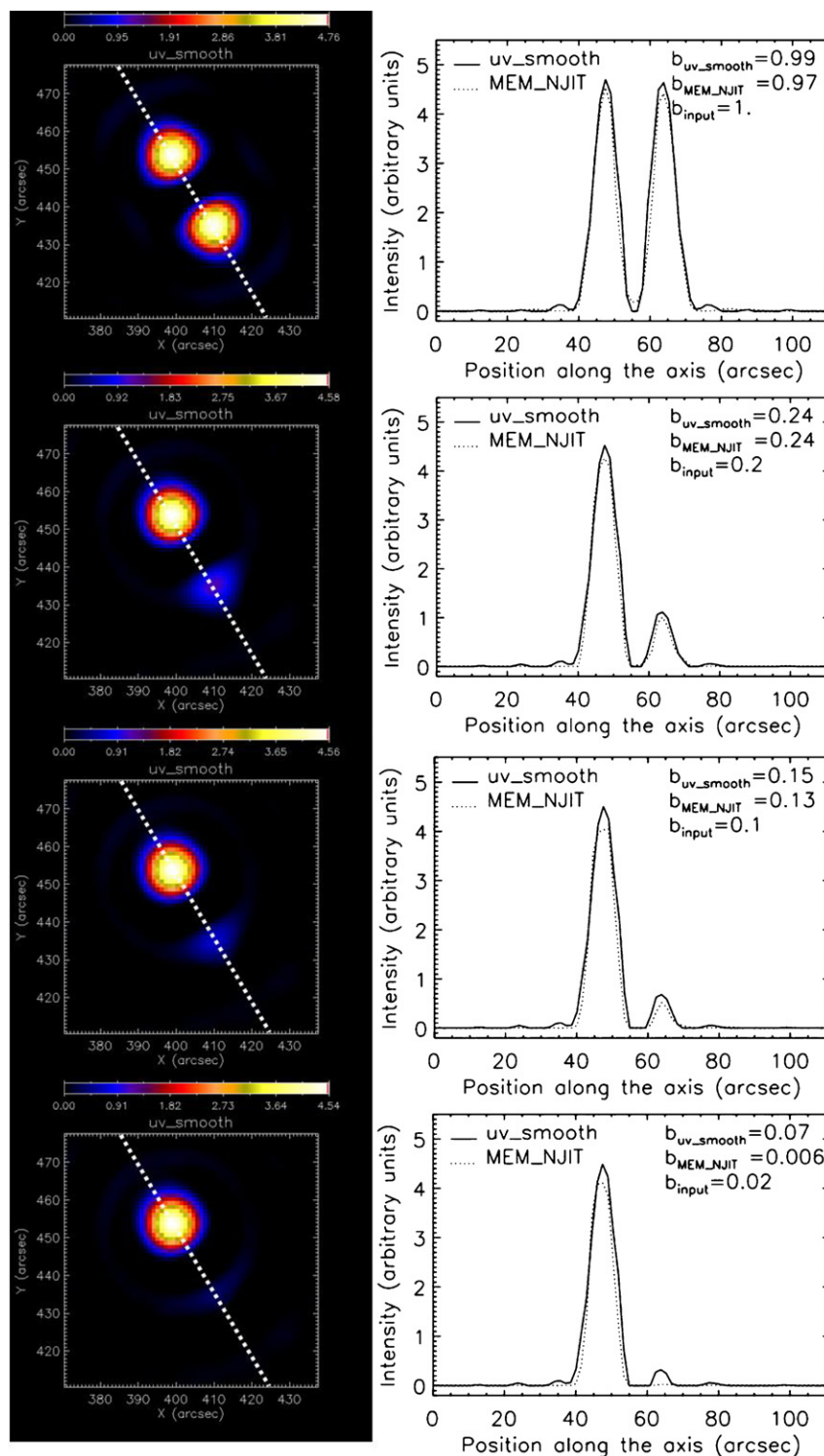
Figure 5. Left column: reconstructed maps, using the `uv_smooth` method, for two circular Gaussian "footpoints" with varying brightness ratio $b = (1, 0.2, 0.1, 0.02)$. Right column: intensity along the line joining the centers of the two sources, for recoveries using the `uv_smooth` method (solid line) and the MEM–NJIT method (dotted line).

(A color version of this figure is available in the online journal.)

a threshold-based filter was applied to the resulting images in order to eliminate weak (and likely spurious) intensity components in the field of view.

The first row of Figure 6 shows the results for the 2002 February 20 double footpoint source, for which the "initial" image was constructed using `uv_smooth`. By contrast with the double Gaussian case considered in the previous subsection (Figure 4), the sources here have spatial frequencies significantly smaller than the largest sampled spatial frequency, enabling a higher fidelity in the reconstruction of the source sizes by `uv_smooth`. As a result, the overall morphology of the source is well recovered by `uv_smooth`; by contrast, the MEM–NJIT
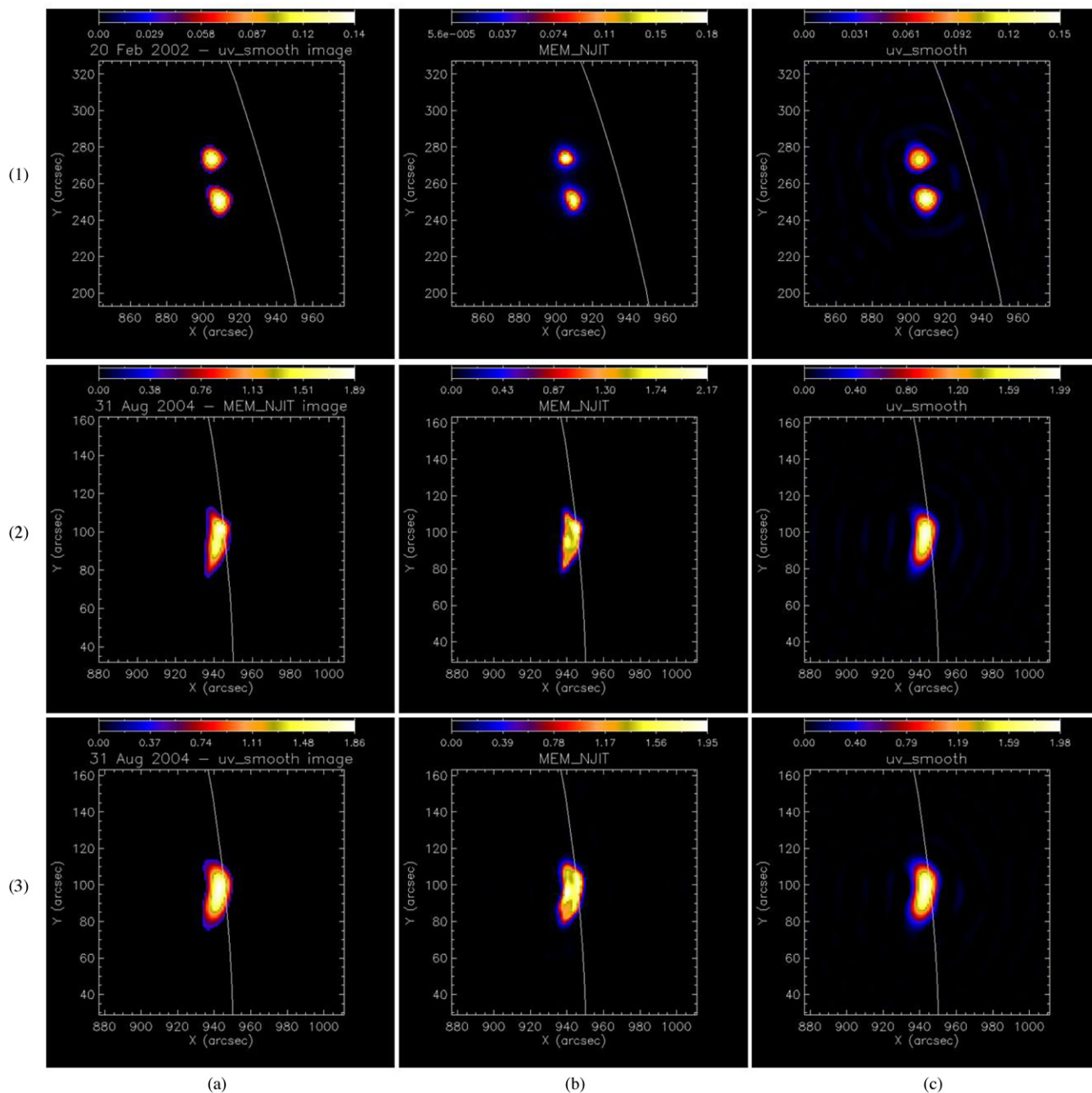
Figure 6. Comparison of image reconstruction methods for simulated source maps based on actual flare images. From top to bottom, the initial images in column (a) show: (1) double footpoint source based on an image of the 2002 February 20 event (energy range $\epsilon = 22$–26 keV), constructed using `uv_smooth`; (2) an extended source, based on an image of the 2004 August 31 event (energy range $\epsilon = 10$–12 keV), constructed using MEM–NJIT; and (3): an extended source, based on an image of the *same* 2004 August 31 event, in the same energy channel, constructed using `uv_smooth`. Column (b) shows the images reconstructed using MEM–NJIT, while column (c) shows the images reconstructed using `uv_smooth`. The field of view is (128 arcsec × 128 arcsec).

(A color version of this figure is available in the online journal.)

method substantially underestimates the source sizes (although it well reproduces the *locations* of the two footpoints).

The second and third rows of Figure 6 show the results for the extended source case of 2004 August 31 (energy range $\epsilon = 10$–12 keV). The "original" image for the second row was based on the image recovered from the *RHESSI* data using MEM–NJIT; the "original" image in the third row was based on the image recovered using `uv_smooth`. It is apparent that `uv_smooth` rather faithfully reproduces the flare morphology, both for the case in which the original image is based on the `uv_smooth` algorithm and for the case in which the original

image is based on the MEM–NJIT algorithm. By contrast, in both cases the MEM–NJIT image contains sharper features that are not present in the original image.

We emphasize that the "original" images in the second and third rows of Figure 6 correspond to the *same* actual event. Furthermore, analysis of the MEM–NJIT-based source *using MEM–NJIT itself* does *not* faithfully produce the original image, but rather results in features that are sharper and narrower than that in the "original" source. In contrast, the `uv_smooth` method not only faithfully reproduce the features in the MEM–NJIT-based image, but also self-consistently reproduces the rather
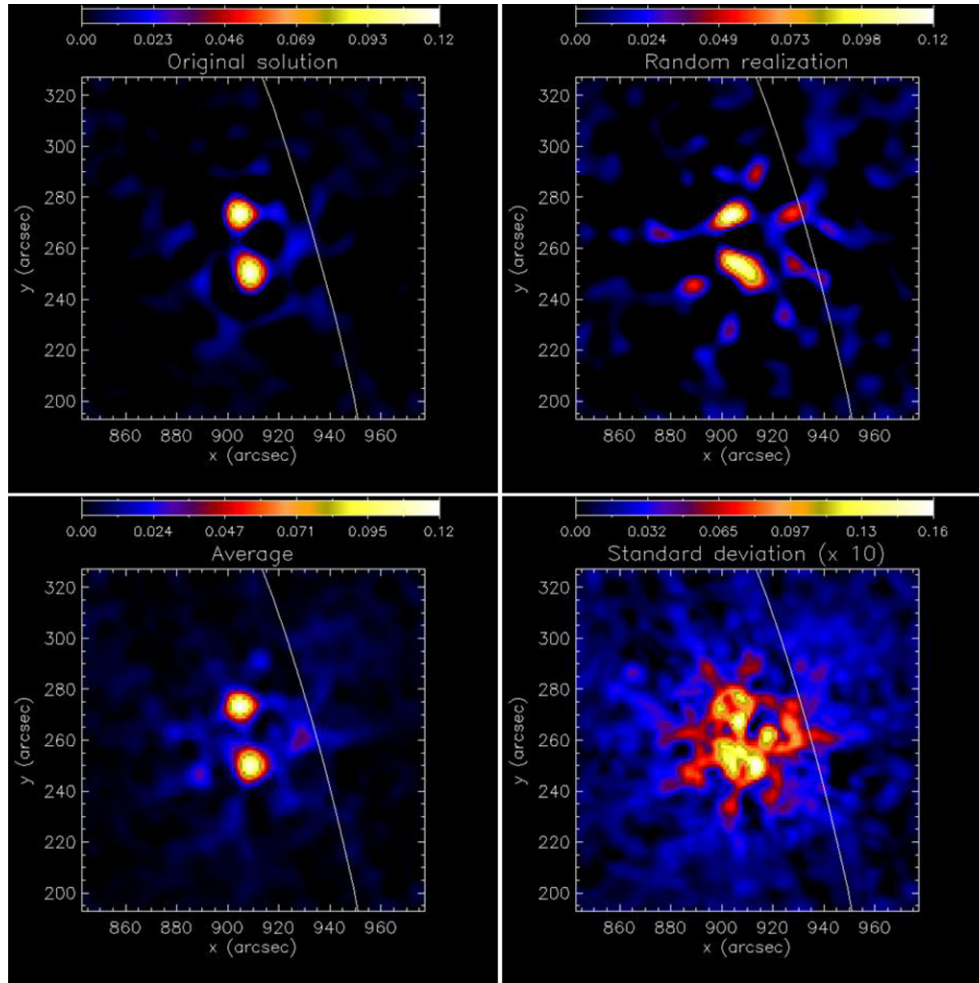
Figure 7. Analysis of the effects of data noise for the 2002 February 20 event. Top panels: images reconstructed from the original visibility data (left) and a noisy realization of this data (right). Bottom panels: Images constructed by combining all (10) noisy realizations—average (left) and standard deviation (right, ×10). The intensity color tables are identical in all plots.

(A color version of this figure is available in the online journal.)

amorphous visibility-based image in the third row that was derived using the `uv_smooth` method itself. It is apparent, therefore, that the sharp features often seen in MEM–NJIT-based images are in all probability *not* representative of the actual flare structure, *but rather are artifacts of the* MEM–NJIT *image reconstruction method*. On the other hand, `uv_smooth` reproduces both high- and low-contrast features if and only if they are present in the actual source.

As a final, crucial, test, we investigate the effects of noise on the ability of the `uv_smooth` method to faithfully reconstruct an image. As our starting points, we took the same 2002 February 20 and 2004 August 31 data used in the construction of Figure 6. In each case, we took the count visibility data and, *without making any adjustments to "improve" the image* (cf. Figure 6), constructed a map of the source. We then added noise, sampled over a ±3σ range, to the visibilities and constructed the image corresponding to each noisy realization. Figures 7 and 8 show the results obtained. In each figure, the top left panel shows the original image and the top right panel an example of a noisy realization, selected as being significantly "deviant" from the original image. The bottom left panel shows the average of 10 image realizations and the bottom right panel shows the 1σ rms noise, scaled by a factor of 10.

These results show that spurious sources (top right panels) *can* arise with the `uv_smooth` method; in this respect, it is no different than any other method when used in conjunction with noisy data. However, unlike many other methods, *the level of noise in the image can be quantitatively estimated*, allowing us to ascertain the reality and/or veracity of any sources that may appear in the field of view.

4. APPLICATION TO DATA

We now illustrate the application of the `uv_smooth` method to actual *RHESSI* data. We selected four flares for study: the 2002 February 20 and 2004 August 31 events used previously in validating the method, an extended-source GOES M3.7 event on 2002 April 15 (00:05:00–00:10:00 UT; previously studied by Veronig & Brown (2004) and Xu et al. (2008)), and the complex and exceptionally well-studied GOES X4.8 event on 2002 July 23 (00:29:10–00:30:19 UT).

Figure 9 shows the images obtained for the 2002 February 20 ($\epsilon = 22$–26 keV), 2002 April 15 ($\epsilon = 12$–14 keV), and 2004 August 31 ($\epsilon = 10$–12 keV) events, using both the MEM–NJIT and `uv_smooth` methods. The images of the 2002 February 20 flare (left column of Figure 9), obtained by both methods, reveal two localized footpoints with similar intensity. By contrast, the images of the other events (2002 April 15 and 2004 August 31) reveal a more extended source structure. These two events have been studied previously by Xu et al. (2008), using a
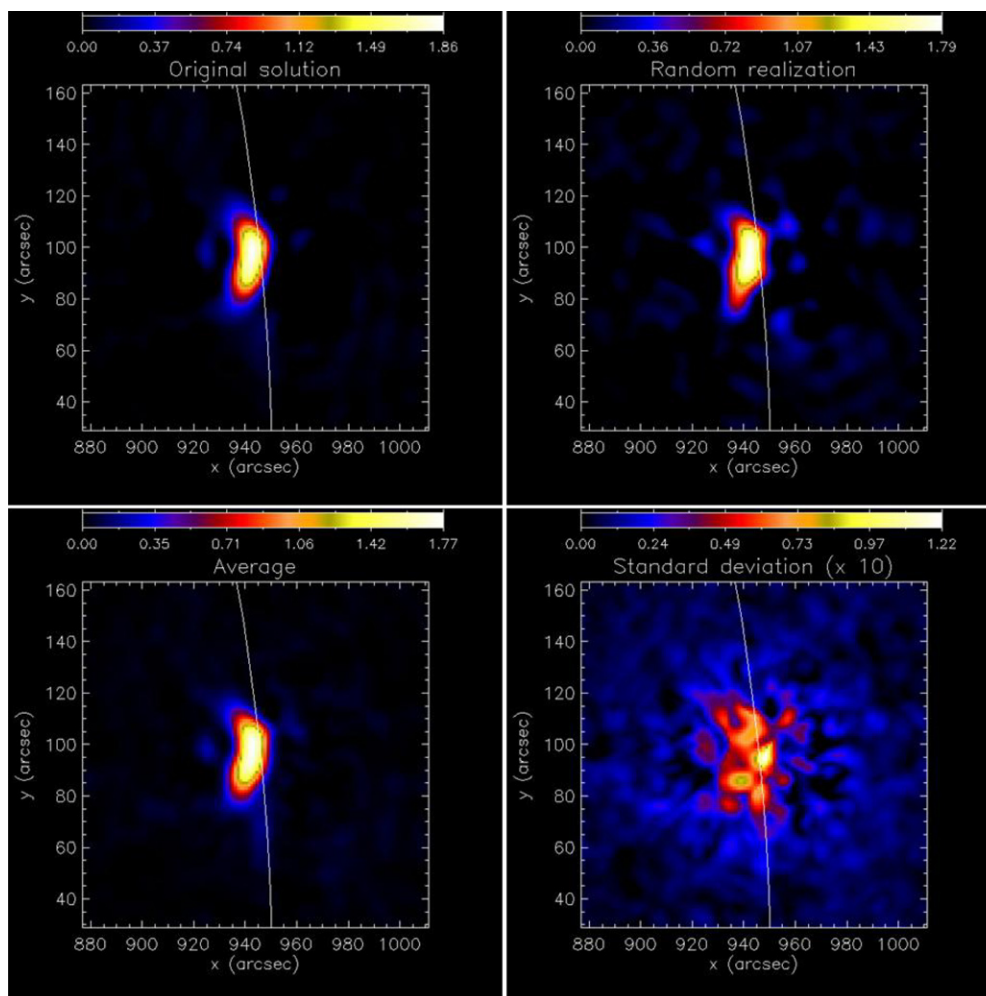
Figure 8. Analysis of the effects of data noise for the 2004 August 31 event. The presentation is the same as in Figure 7.

(A color version of this figure is available in the online journal.)

procedure involving parametric forward-fits to the visibilities sampled by *RHESSI*. The shapes of the sources determined using uv_smooth are very similar to those found using the Clean algorithm (Xu et al. 2008), and are also consistent with the curved-elliptical-Gaussian source structures assumed in the forward-fit analysis by these authors.

We used the images obtained by the uv_smooth method to estimate the "size" of the source along the "axial" direction of brightest emission. In Figure 10, we compare the variation of source "size" with photon energy ϵ with that found by Xu et al. (2008); because the definition of source "size" varies between the two techniques (cf. Equation (20) of Xu et al. 2008), the Xu et al. (2008) results have been scaled to match the definition of source size used in the uv_smooth analysis. Both results show a relatively gradual increase in source size with ϵ. From this behavior, a thermal interpretation for the source was ruled out by Xu et al. (2008), and they were also able to deduce both the size and density of the electron acceleration region in each source. In a future paper, we intend to use uv_smooth to perform a similar analysis, and to explore the attendant physical implications, more fully.

The application of the method to the 2002 July 23 flare, previously studied in a number of papers in a special 2003 issue of *The Astrophysical Journal (Letters*, volume 595), merits special attention. Although this event was sufficiently intense that pulse pileup (Smith et al. 2002) in the *RHESSI* detectors

was significant, this issue is not critical for our present study, which seeks mainly to compare imaging methodologies. We therefore take the visibility data recorded for this event as "truth," and proceed to construct images using uv_smooth, for the same time interval and energy channels used in the imaging spectroscopy analysis of Emslie et al. (2003), who used the Clean algorithm to construct the various source maps, and who identified four prominent features in the flare—a coronal source with a relatively soft spectrum, and three compact sources (see the 36–41 keV panel in Figure 11). Two of these, labeled "northern" and "southern," were identified as footpoint sources; a third compact source, labeled "middle," was tentatively identified as another footpoint on the basis of context information at other wavelengths (e.g., Hα, Emslie et al. 2003).

Figure 11 reproduces the Clean-based images from Emslie et al. (2003). These images were constructed using a "uniform" weighting scheme, which gives progressively increased weight to detectors with finer resolution. This compensates for the greater areal coverage of the annulus of the (u, v) plane sampled by these collimators (see Figure 1), thereby resulting in a near-uniform sampling across the (u, v) plane.

Figure 12 shows a comparison of the uv_smooth results (bottom half of figure) with results obtained with the Clean algorithm using "natural" weighting, in which counts from all detectors are given equal weight. Such a weighting is more appropriate for comparison with the uv_smooth procedure,
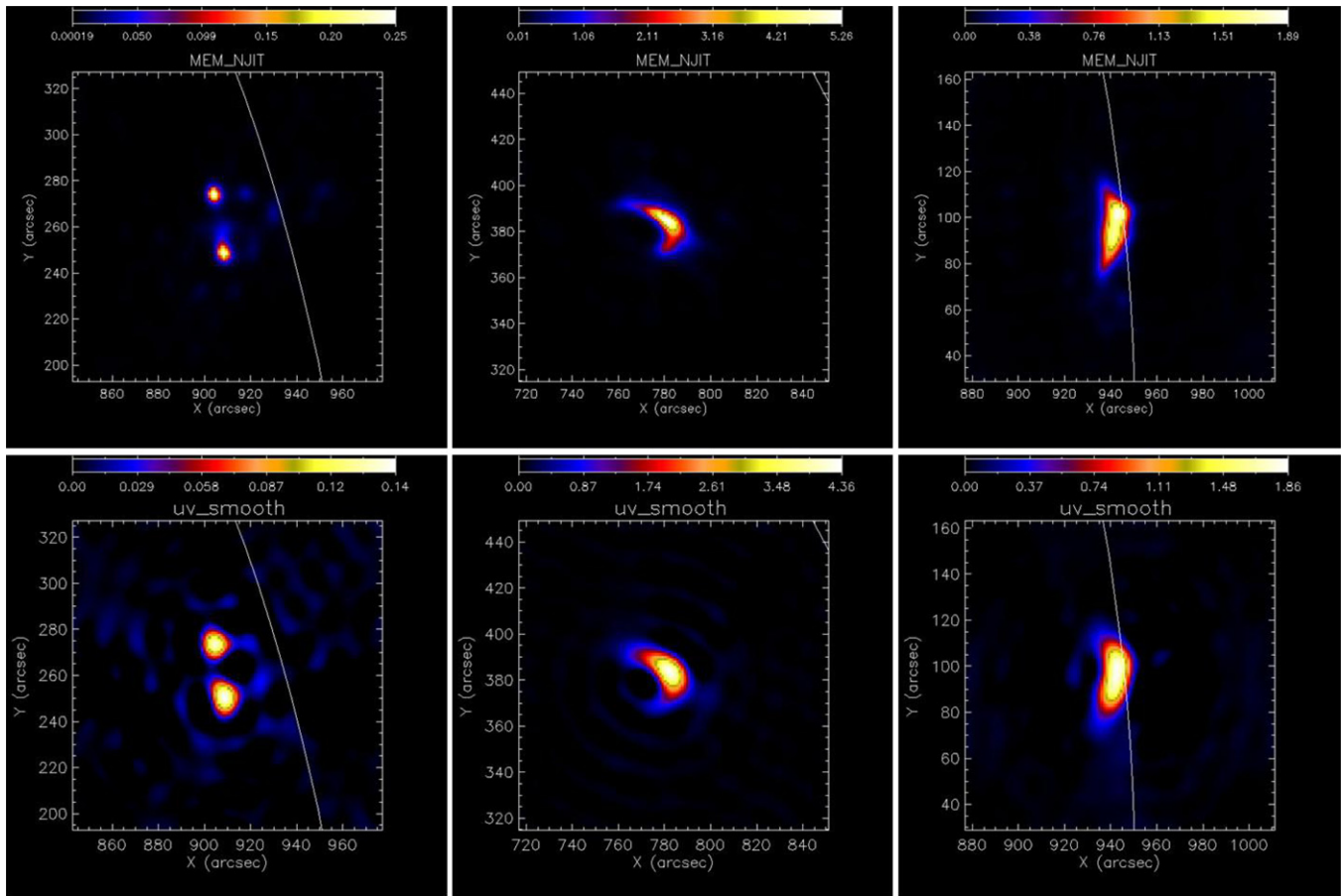
Figure 9. Reconstructed images for the flares of 2002 February 20 (left column; 22–26 keV), 2002 April 15 (middle column; 12–14 keV), and 2004 August 31 (right column; 10–12 keV). The top row shows the images reconstructed using MEM–NJIT, and the bottom row the images reconstructed using uv_smooth.

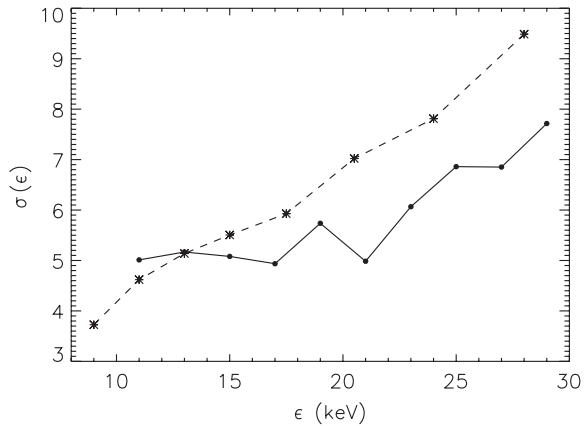(A color version of this figure is available in the online journal.)

Figure 10. Variation of source size with photon energy ϵ for the 2002 April 15 event. The dashed line shows the results of Xu et al. (2008; scaled to match the definition of "size" used in the current work); the solid line shows the results obtained using uv_smooth.

in which visibilities at all sampled points are used in the interpolation algorithm. The overall morphology of the flare is confirmed in all sets of images (Figures 11 and 12). However, there are some crucial differences between the sets of images.

1. In the natural-weight Clean and uv_smooth images (Figure 12), the "middle" source that appears in the uniform-weighting Clean images (Figure 11) is blended with the "northern" source over most of the energy range. This indicates that the appearance of this source in the natural-weight Clean images (Figure 11) may be an artifact of that method. The "northern" source, then, is perhaps more extended that as revealed by the uniform-weight Clean images and it should be noted that Dennis & Pernak (2009) caution not to use Clean "for extended sources, especially in the presence of compact sources." Closer examination of the natural-weight Clean images and the uv_smooth images (Figure 12) indicates emission extending along a curved locus joining the "northern" footpoint with the "southern" one, strongly suggestive of target material that has "evaporated" into a coronal loop in response to flare heating (see, e.g., Mariska et al. 1989). An analysis of the temporal evolution of the sources, beyond the scope of the present work, is necessary to address this issue satisfactorily.

2. The "coronal" source, which is visible only up through the 36–41 keV channel in the Clean images, is apparent all the way up to 85 keV in both the natural-weight Clean images and the uv_smooth images (Figure 12). Its absence in the uniform-weight Clean images (Figure 11) at energies above 41 keV is a consequence of both sampling and dynamic range issues—at higher count energies, the footpoints have a higher intensity per pixel and the uniform-weight Clean algorithm, with its reduced weighting of (u, v) points corresponding to smaller spatial scales, simply ignores the relatively weak coronal source in its synthesis of the image through systematic assembly of the brightest pixels in the field of view. By contrast, using natural weights in the Clean algorithm, or using uv_smooth, places equal weight on the
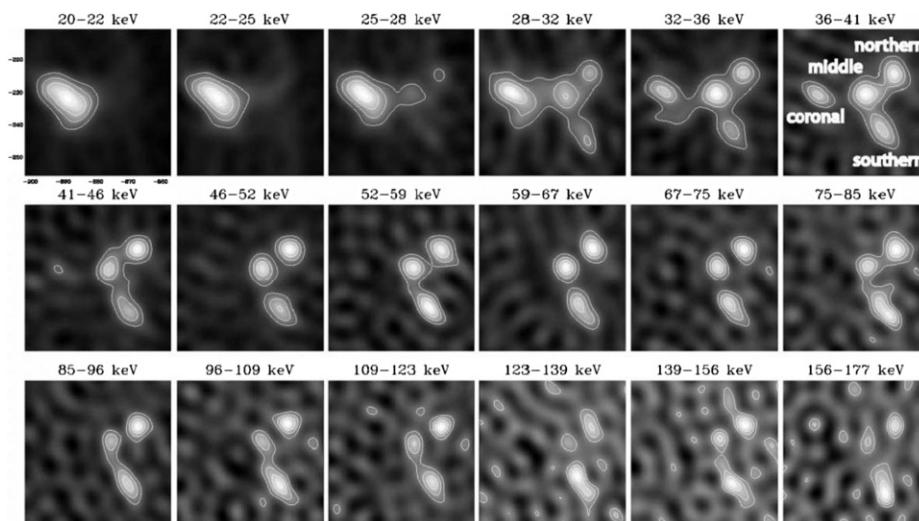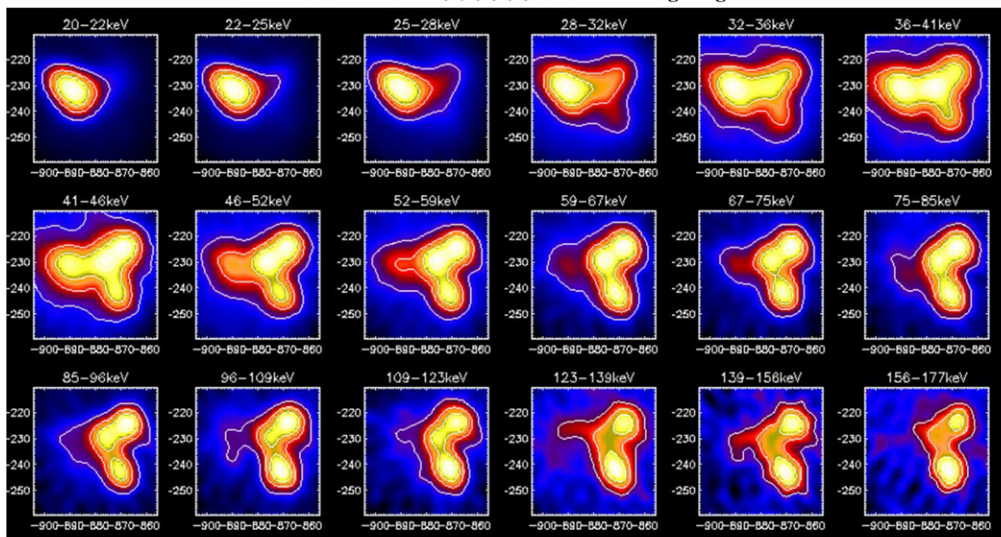
Figure 11. Images obtained for the 2002 July 23 event, using the Clean algorithm with *uniform* detector weighting (Emslie et al. 2003, reproduced by permission of the AAS). The contour levels are set at 30%, 50%, 70%, and 90% of peak intensity.
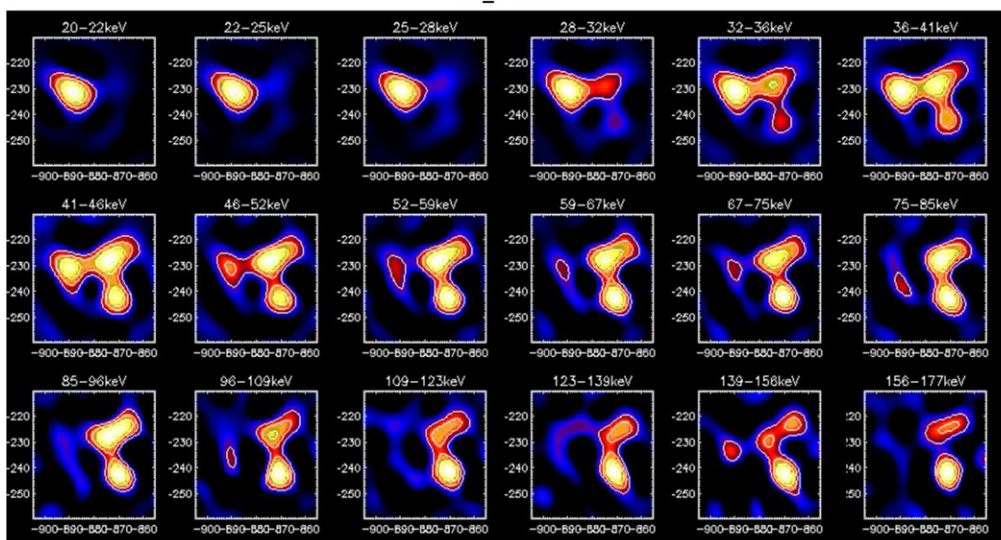

Figure 12. Comparison of the images obtained for the 2002 July 23 event, using both the Clean algorithm with *natural* detector weighting (top panels), and uv_smooth (bottom panels). The contour levels are the same as in Figure 11.

(A color version of this figure is available in the online journal.)

information from all samples visibilities, including those at large radii in the (u, v) plane (Figure 1). Such a data sampling preserves information on *all* compact sources in the field of view, so that using natural weights in Clean, or using `uv_smooth`, continues to map the coronal source even when, per unit area, its brightness is much smaller than that of the compact footpoints.

A key result from the above comparison exercise is that the `uv_smooth` method generates images with very similar morphology to those produced by the Clean algorithm with *natural* weighting. Moreover, because of its reliance on FFT techniques, rather than repetitive sampling of a "dirty" image, `uv_smooth` does so with much greater computational efficiency. Furthermore, since `uv_smooth` uses information provided by Fourier components interpolated between observed (u, v) values, features produced by the `uv_smooth` method are generally sharper than those produced by Clean, even when natural weighting is employed (Figure 12). These results bode well for the use of `uv_smooth` in many scientific investigations, and indeed we intend to revisit the imaging spectroscopy analysis of Emslie et al. (2003) for the 2002 July 23 event, using the `uv_smooth` maps as a starting point.

5. DISCUSSION AND CONCLUSIONS

The best physics starts with the best images. Reconstructing accurate and reliable images from a finite, sparsely distributed set of visibilities is key to addressing many of the issues confronting astronomical imaging spectroscopy, especially that carried out using instrumentation that realizes visibilities as a "primary" form of data.

For relatively simple sources, the key elements of an imaging method include the ability to correctly and robustly determine:

1. the *location* of the peak intensity in a source;
2. the absolute photometric *intensity* of a source;
3. the *size* and *shape* of a source, for both compact and extended sources; and
4. the relative brightness of a source in the presence of other sources exhibiting a significant *dynamic range*.

We have demonstrated a new method of image reconstruction that

1. is based on visibilities (two-dimensional spatial Fourier components), the data form most "native" to *RHESSI*'s rotating modulation collimator imaging technique;
2. replaces the unknown visibilities at non-sampled (u, v) points with smoothly varying values; and
3. uses an iterative routine incorporating a positivity constraint on the image to provide visibilities that taper gradually to zero outside the sampling domain.

The method

1. faithfully, accurately, and robustly reproduces the *locations*, *sizes,* and *shapes* of sources in the field of view, even when multiple sources, with differing geometries, are present;

2. reproduces the *photometric intensity* of individual compact sources to within a few percent; and
3. reproduces the *intensity ratio* of multiple compact sources, to within an accuracy of a few percent for sources of comparable brightness to a factor of $\sim$30% for sources with a 10:1 brightness ratio.

Although a full scientific analysis of the images produced by `uv_smooth` is beyond the scope of the present paper, the method shows promise for the inference of key physical properties of the accelerated electrons that produce the observed bremsstrahlung radiation and we submit that the images resulting from this new technique are well suited to further analysis. Moreover, because FFT is the core of the image reconstruction algorithm, the `uv_smooth` technique is at least an order of magnitude *faster* to use than previous methods, such as Clean or MEM–NJIT. Also, as was demonstrated in Section 4, the `uv_smooth` method is also a *robust* method, applicable to a wide variety of source structures and count levels. Lastly, we wish to stress that the visibilities used as input data to the method can be either count-based or, via a spectral inversion algorithm (Piana et al. 2007), electron-flux-based, or indeed based on any pertinent data set. An IDL algorithm based on the `uv_smooth` method, entitled `uv_smooth`, has been incorporated into the SSW tree.

REFERENCES

Aschwanden, M. J. 2002, Sol. Phys., 210, 193
Bong, S. C., Lee, J., Gary, D. E., & Yun, H. S. 2006, ApJ, 636, 1159
Dennis, B. R., & Pernak, R. L. 2009, ApJ, 698, 2131
Emslie, A. G., Kontar, E. P., Krucker, S., & Lin, R. P. 2003, ApJ, 595, L107
Hogbom, J. A. 1974, A&A, 15, 417
Hurford, G. J., et al. 2002, Sol. Phys., 210, 61
Lin, R. P., et al. 2002, Sol. Phys., 210, 3
Mariska, J. T., Emslie, A. G., & Li, P. 1989, ApJ, 341, 1067
Piana, M., & Bertero, M. 1997, Inverse Probl., 13, 441
Piana, M., Massone, A. M., Hurford, G. J., Prato, M., Emslie, A. G., Kontar, E. P., & Schwartz, R. A. 2007, ApJ, 665, 846
Piña, R. K., & Puetter, R. C. 1993, PASP, 105, 630
Schwartz, R. A., Csillaghy, A., Tolbert, A. K., Hurford, G. J., McTiernan, J., & Zarro, D. 2002, Sol. Phys., 210, 165
Smith, D. M., et al. 2002, Sol. Phys., 210, 33
Thomson, A. R., Moran, J. M., & Swenson, G. W. 2001, Interferometry and Synthesis in Radio Astronomy (2nd ed.; New York: Wiley)
Veronig, A. M., & Brown, J. C. 2004, ApJ, 603, 117
Wahba, G. 1990, Spline Models for Observational Data (Philadelphia, PA: SIAM)
Xu, Y., Emslie, A. G., & Hurford, G. J. 2008, ApJ, 673, 576
Youla, D. C. 1987, Image Recovery: Theory and Applications, in Mathematical Theory of Image Restoration by the Method of Convex Projections, ed. H. Stark (New York: Academic)